



1 **Spatial and temporal variations in basal melting at Nivlisen ice**
2 **shelf, East Antarctica, derived from phase-sensitive radars**

3 **Katrin Lindbäck¹, Geir Moholdt¹, Keith W. Nicholls², Tore Hattermann¹, Bhanu Pratap³,**
4 **Meloth Thamban³, Kenichi Matsuoka¹**

5 ¹ Norwegian Polar Institute, Framsentret, Postboks 6606, Langnes, 9296 Tromsø, Norway.

6 ² British Antarctic Survey, Natural Environmental Research Council, High Cross, Madingley Rd,
7 Cambridge CB3 0ET, UK.

8 ³ ESSO-National Centre for Polar and Ocean Research, Ministry of Earth Sciences, Headland
9 Sada, Vasco-da-Gama, Goa 403 804 , India.

10

11 *Correspondence to:* Katrin Lindbäck (katrin.lindback@npolar.no)

12

13 **Abstract**

14 Thinning rates of ice shelves vary widely around Antarctica and basal melting is a major
15 component in ice shelf mass loss. In this study, we present records of basal melting, at unique
16 spatial and temporal resolution for East Antarctica, derived from autonomous phase-sensitive
17 radars. These records show spatial and temporal variations of ice shelf basal melting in 2017 and
18 2018 at Nivlisen, central Dronning Maud Land. The annually averaged melt rates are in general
19 moderate (~ 0.8 m yr⁻¹). Radar profiling of the ice-shelf shows variable ice thickness from
20 smooth beds to basal crevasses and channels. The highest melt rates (3.9 m yr⁻¹) were observed
21 close to a grounded feature near the ice shelf front. Daily time-varying measurements reveal a
22 seasonal melt signal 4 km from the ice shelf front, at an ice draft of 130 m, where the highest
23 daily melt rates occurred in summer (up to 5.6 m yr⁻¹). This seasonality indicates that summer-
24 warmed ocean surface water was pushed by wind beneath the ice shelf front. We observed a
25 different melt regime 35 km into the ice-shelf cavity, at an ice draft of 280 m, with considerably
26 lower melt rates (annual average of 0.4 m yr⁻¹) and no seasonality. We conclude that warm deep



27 ocean water at present has limited effect on the basal melting of Nivlisen. On the other hand, a
28 warming in surface waters, as a result of diminishing sea-ice cover has the potential to increase
29 basal melting near the ice-shelf front. Many ice shelves like Nivlisen are stabilized by pinning
30 points at their ice fronts and these areas may be vulnerable to future change.

31

32 **1 Introduction**

33 The Antarctic contribution to global sea-level rise has increased by a factor of five in the
34 past two decades (The IMBIE Team, 2018). This rapid increase in the overall mass deficit is
35 mostly caused by several retreating and thinning glaciers in West Antarctica that lost buttressing
36 forces from their shrinking ice shelves (De Angelis and Skvarca, 2003; Joughin et al., 2014;
37 Rignot et al., 2014). Over 80 % of the grounded ice in Antarctica drains out into floating ice
38 shelves (Dupont and Alley, 2005). The thinning rates of these ice shelves vary widely around the
39 continent (Paolo et al., 2015). The mass balance of an ice shelf is the sum of the ice gain and
40 loss; ice gain comprises the advective input of grounded ice upstream, snow accumulation, and
41 marine ice accretion, and ice loss encompasses basal melting from the ocean and iceberg calving
42 (Bamber et al., 2018). A negative mass balance can affect ice-shelf stability: where the mass loss
43 reduces back stress on grounded ice upstream of the ice shelf, leading them to flow faster (Reese
44 et al., 2018). Understanding controls on the mass balance of ice shelves around Antarctica is
45 therefore key to gaining a better understanding of the continent's present and future contribution
46 to global sea-level rise.

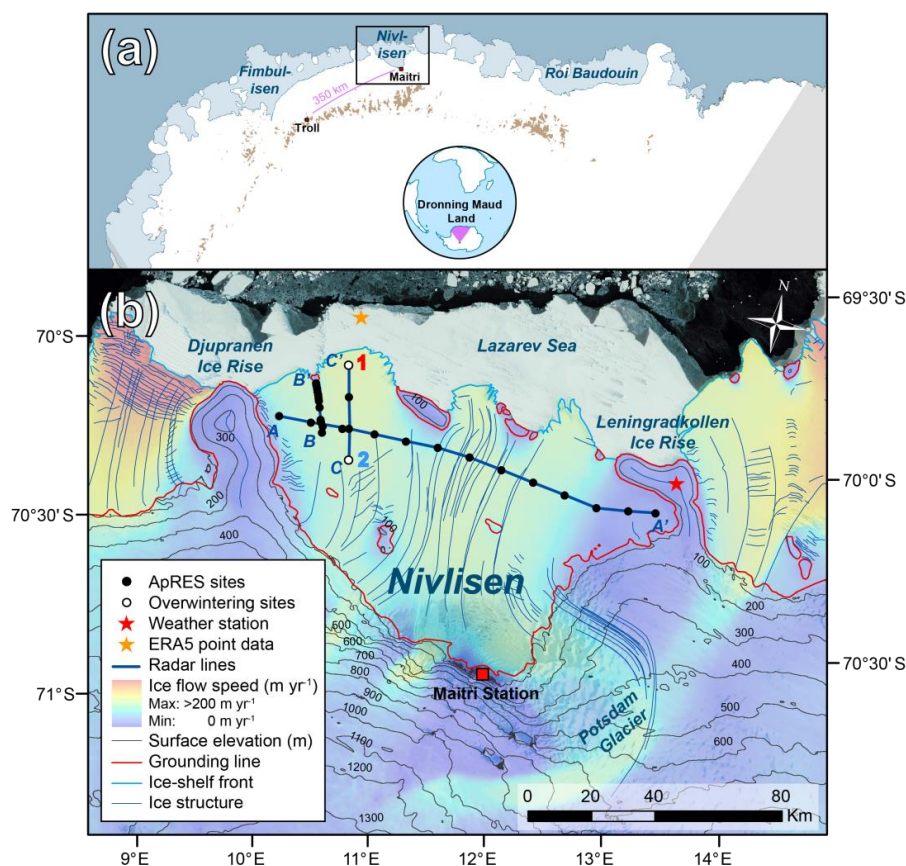
47 Iceberg calving occurs irregularly in time and can have dramatic effects on ice shelf mass
48 balance when it occurs (Hogg and Gudmundsson, 2017). At present, however, basal melting is
49 the largest mass-loss process for Antarctic ice shelves (Depoorter et al., 2013; Rignot et al.,
50 2013). Melting of ice shelves by the ocean is not uniform and depends on the ocean properties in
51 the vicinity of the ice shelf, the topography of both the ocean bed and the ice-shelf base. Jacobs
52 et al. (1992) described three different modes of melting: In mode 1, ocean water with
53 temperatures at the surface freezing point provides heat for basal melting of deeper parts of the
54 ice base, because the pressure-melting point of the ice is decreased to lower temperatures at
55 depth. Since these cold shelf waters provide a limited source of ocean heat (Darelius and Sallée,



56 2017), average melt rates are often low for the largest ice shelves (e.g., 0.3 m yr⁻¹ for Ronne Ice
57 Shelf with; Rignot et al., 2013). In addition, substantial marine ice accretion occurs when the
58 rising melt plume from the grounding zone super-cools and refreezes on the ice-shelf base at
59 shallower depths (Joughin and Vaughan, 2004).

60 The rapid retreat and high thinning rates of glaciers in the Amundsen Sea sector of West
61 Antarctica are thought to be driven by an increased presence of warm circumpolar deep water
62 below the ice shelves (Pritchard et al., 2012; Rignot et al., 2013), referred to as melt mode 2 in
63 Jacobs et al. (1992). Circumpolar deep water surrounds the Antarctic continent, flowing
64 clockwise with the Antarctic Circumpolar Current and is abundant near the continental shelf of
65 West Antarctica. Circumpolar deep water accesses the deep bases of ice shelves directly through
66 cross-continental submarine troughs, causing high melt rates; for example Rignot et al. (2013)
67 found Pine Island Ice Shelf to have an average melt rate of 16 m yr⁻¹. In East Antarctica, basal
68 melting has been linked to circumpolar deep water intrusion only at Tottem Ice Shelf, where
69 annual basal melt rates reached ~11 m yr⁻¹ (Rignot et al., 2013; Rintoul et al., 2016). Farther
70 west, in the Weddell Sea sector a cooler modified version of circumpolar deep water is advected
71 along the coast (Dong et al., 2016; Ryan et al., 2016).

72 Ice shelves can also melt in the vicinity of their ice fronts when summer-warmed
73 Antarctic surface water is pushed by wind and tides under ice shelves (Jenkins and Doake, 1991;
74 Makinson and Nicholls, 1999; Sverdrup, 1954; Zhou et al., 2014). Jacobs et al. (1992) refer to
75 this as melt mode 3. Antarctic surface water has only recently been observed at Ross Ice Shelf
76 (Malyarenko et al., 2019; Stern et al., 2013; Stewart et al., 2019) and at Fimbulisen (Hattermann
77 et al., 2012), suggesting it may be an important process in basal melting. Spatial patterns and
78 relative magnitudes of all these three modes remain largely unknown. Numerical modelling,
79 however, indicates that the response of basal melting in the future strongly depends on the
80 surface air warming (Kusahara and Hasumi, 2013). Future basal melting in Antarctica will
81 therefore reflect the integrated response to remotely changes in sub-surface circumpolar deep
82 water temperatures and the coastal processes that control its access to the continental shelf
83 (Thompson et al., 2018) and the local upper ocean heat supply. The detailed interplay of these
84 processes today and in a future climate are still a major source of uncertainty when evaluating
85 the response of the Antarctic Ice Sheet to climate change (Adusumilli et al., 2018).



86
87

88 **Figure 1.** Study area: (a) Dronning Maud Land coast, with Maitri Station, Troll Station, Nivlisen, Fimbulisen, and
89 Roi Baudouin Ice Shelf. (b) Nivlisen ice shelf with surrounding areas. Study sites, where ApRES and stakes for ice
90 speed and surface mass balance were made, ApRES overwintering sites (no. 1 called “seaward” and no. 2 called
91 “landward”), and low-frequency radar profiles (A, B, and C). Satellite derived ice speed (Rignot et al., 2011),
92 surface elevation (m a.s.l.; Howat et al., 2019), grounding line, ice-shelf front (Mouginot et al., 2017), and ice
93 structure (Goel et al, in review) are also shown. Background image is Landsat image mosaic (Bindschadler et al.,
94 2008) and grid coordinate system WGS-84.
95

96 In this study, we measured basal melting at Nivlisen (70° S, 12° E), Dronning Maud
97 Land, East Antarctica, using autonomous phase-sensitive radio-echo sounders (ApRES; Fig. 1).
98 Phase-sensitive radars uses a technique where the phase of individual internal ice reflectors is
99 tracked, yielding time series of ice thickness change at high-resolution (~1 mm) over short time



100 intervals (Corr et al., 2002; Nicholls et al., 2015) and have been used to measure basal and
101 englacial properties of ice at several locations around Antarctica (e.g., Davis et al., 2018; Jenkins
102 et al., 2006; Marsh et al., 2016; Stewart et al., 2019), and recently also in Greenland (Vaňková et
103 al., 2018). Our objective is to study the spatial and temporal variations of basal melting to
104 explain them using: (1) radar profiles of ice thickness, (2) in situ measured and satellite-derived
105 ice flow speed and surface mass balance, (3) atmospheric forcing from reanalysis data, sea-ice
106 distributions, and ocean tides. The data imply that different melt modes were present at Nivlisen.
107 Our in situ measured data of basal melting complements satellite-derived maps of spatially-
108 smoothed time-averaged melt rates, and will be a valuable source of data for validation of ice
109 shelf and ocean models.

110

111 **2 Study area**

112 In the following section, we summarize the geographical, glaciological, and
113 oceanographic settings of the study area. Dronning Maud Land covers a large area of East
114 Antarctica, and its 2000-km-long coast is characterized by extensive ice shelves interspersed
115 with numerous ice rises and ice-sheet promontories (Fig. 1a). Individual ice shelves are relatively
116 small, but extend close to, or even beyond, the continental-shelf break (Heywood et al., 1998).
117 Satellite-derived ice-shelf averaged net basal melt rates in Dronning Maud Land vary from near
118 zero to 7 m yr^{-1} (2003 to 2008; Rignot et al., 2013). The interior of this region is partly separated
119 by high mountains, causing steep slopes from the continental plateau towards the coastal areas
120 (Howat et al., 2019). Nivlisen is located in central Dronning Maud Land, 400 km east of
121 Fimbulisen (Fig. 1a), the largest ice shelf in the area. 100 km south of Nivlisen lies the Wohlthat
122 Massif, with a maximum elevation of $\sim 3000 \text{ m}$ above sea level (a.s.l.). Between the mountain
123 massif and the ice shelf lies the Schirmacher Oasis, an ice-free area with a maximum elevation of
124 $\sim 250 \text{ m a.s.l.}$, with numerous lakes and ponds. The drainage basin of Nivlisen ($27\,700 \text{ km}^2$),
125 including the grounded ice that drains to the ice shelf, has an ice volume equivalent to 8 cm of
126 global sea-level rise (Rignot et al., 2019).

127 Nivlisen has an areal extent of $\sim 7300 \text{ km}^2$ and forms a closed embayment between two
128 larger promontory-type ice rises, Djupranen and Leningradkollen (Fig. 1b). Ice rises are
129 locations where ice-shelf flow is diverted around the grounded ice and are miniature ice caps



130 with their own flow fields from the summit (Matsuoka et al., 2015). Ice rumples are smaller
131 features that impose a disturbance on the ice shelf flow, causing the ice to thicken upstream with
132 extensive crevassing in the grounding zone. Such grounded features are known to play vital roles
133 in ice-shelf and ice-sheet dynamics over various timescales. For example, un-grounding of an ice
134 rumples within the ice shelves of Pine Island and Thwaites Glacier is thought to be a major cause
135 of the ongoing rapid retreat and thinning (Favier et al., 2012; Gladstone et al., 2012; Jenkins et
136 al., 2010). Bawden Ice Rise near the edge of the Larsen C Ice Shelf helps maintain the shelf,
137 despite the collapse of neighbouring Larsen A and B ice shelves (Borstad et al., 2013; Holland et
138 al., 2015). Nivlisen is grounded at a series of smaller ice rises and rumples near the present ice
139 front, as well as at a few ice rumples in the middle of the ice shelf (Moholdt and Matsuoka,
140 2015). The bathymetry under the ice shelf is unknown.

141 The average ice shelf flow speed is 80 m yr^{-1} (Rignot et al., 2011). Potsdam Glacier
142 drains into Nivlisen from the southeast, with an average ice thickness of $\sim 1000 \text{ m}$ (Fretwell et
143 al., 2013) and ice flow speed of $\sim 50 \text{ m yr}^{-1}$ (Anschütz et al., 2007; Rignot et al., 2011). The
144 satellite-derived estimate of the grounding-line flux for Nivlisen was $3.9 \pm 0.8 \text{ Gt yr}^{-1}$
145 (2007–2008; Rignot et al., 2013). Elevated topography of the ice rises causes highly-variable
146 local climate and surface mass balance (Lenaerts et al., 2014). In addition, Nivlisen has large
147 surface mass balance transitions from being positive in the firn area near the ice front to being
148 negative in the blue-ice area near the grounding zone, with increased wind erosion, evaporation,
149 and sublimation due to katabatic winds (Horwath et al., 2006). Near the grounding zone, summer
150 surface melting is sufficient to form supraglacial lakes and streams that may occasionally drain
151 through the ice shelf (Kingslake et al., 2015), making Nivlisen potentially sensitive to
152 hydrofracturing (Lenaerts et al., 2017). Rignot et al. (2013) estimated the surface mass balance to
153 be $1.8 \pm 0.3 \text{ Gt yr}^{-1}$ (average 1979–2010) and the average calving flux to be $1.3 \pm 0.4 \text{ Gt yr}^{-1}$
154 (2007–2008). Together with the grounding-line flux mentioned earlier and a slightly positive net
155 mass balance of 0.6 Gt yr^{-1} (2003–2008) results in a residual net basal melt of 3.9 Gt yr^{-1} , or an
156 average basal melt rate of $0.5 \pm 0.2 \text{ m yr}^{-1}$ (Rignot et al., 2013). Thus, basal melting comprises
157 $\sim 75 \%$ of the total mass losses, with the remaining $\sim 25 \%$ coming from iceberg calving.

158 The continental shelf extends $\sim 100 \text{ km}$ north of Nivlisen into the Lazarev Sea, and is
159 roughly 500 m deep (Arndt et al., 2013). Carbon dating of laminated sediments near the ice shelf



160 suggests that the continental shelf was deglaciated ~11 kyr ago (Gingele et al., 1997). At the
161 eastern border of Lazarev Sea lies Astrid Ridge (~12° E), an undersea bathymetric feature
162 extending from the Antarctic margin northward to ~65° S. Farther east lies Gunnerus Ridge
163 (~33° E), where circumpolar deep water is entrained, which is then cooled and modified to
164 become warm deep water (Dong et al., 2016; Ryan et al., 2016). Warm deep water flows
165 westward along the continental slope and is entrained into the Weddell Gyre. The Southern
166 Ocean, including the Weddell Sea, has warmed over recent decades (Gille, 2002; Schmidtko et
167 al., 2014) with the changes driven primarily by anthropogenic climate warming (Swart et al.,
168 2018). Sea-ice cover has increased slightly since 1979 around Antarctica in general (De Santis et
169 al., 2017), however extreme changes have occurred in recent years with record maxima three
170 years in a row (2012 to 2014), followed by record summertime minimum in 2016 and 2017
171 (Shepherd et al., 2018; Stuecker et al., 2017; Turner et al., 2015). Sea-ice fluctuations are
172 strongly correlated with the dominant modes of Southern Hemisphere climate variability (Kwok
173 et al., 2016; Kwok and Comiso, 2002), although further studies are needed to understand the
174 drivers behind these fluctuations (Turner 2017). An increase in the seasonality of the easterly
175 winds has been observed (Hazel and Stewart, 2019) and this may affect the formation and export
176 of sea ice and the transport of surface waters and warm deep water to the continental shelf. All
177 these pan-Antarctic observations may affect ocean water flow and then ice-shelf thinning in
178 Dronning Maud Land, which remain largely unknown.

179

180 **3 Data and Methods**

181 We conducted three field campaigns on Nivlisen and adjacent ice rises during Antarctic
182 austral summers, from mid-November until end of December, 2016 to 2018, with logistic
183 support from the Indian Maitri Station and Norwegian Troll Station (Fig. 1a). We measured basal
184 melting under Nivlisen using two ApRES systems (200–400 MHz), developed by the British
185 Antarctic Survey (British Antarctic Survey, 2018; Nicholls et al., 2015). Below, we describe the
186 methods used to collect the ApRES data and process them to derive basal melt rates (Sect. 3.1).
187 We also studied the ice-shelf thickness and basal structure with a low-frequency (5 MHz) radio-
188 echo sounder (Sect. 3.2). Finally, the annual ice flow speed and surface mass balance were
189 measured at stake locations along three profiles on the ice shelf (Sect. 3.3).



190 3.1 Autonomous phase-sensitive radar

191 In December 2016, we installed stakes for measurement of ice speed and surface mass
192 balance at 29 locations on Nivlisen and measured the ice thickness using an ApRES system (Fig.
193 1b): (A) 13 stakes were placed across the ice shelf at a spacing of 10 km (profile A), (2) 10
194 stakes were placed along the ice flow towards a grounded feature near the ice front with a
195 spacing of 1 to 4 km (profile B), and (3) Four stakes were placed along the ice flow out on an ice
196 tongue at a spacing of 10 km (profile C). After the initial measurements, we installed similar
197 ApRES systems at two locations for hourly measurements of basal melting and strain rates over
198 the winter, each powered by a 12 V battery (Fig. 1b): (1) 4 km from the ice-shelf front, called the
199 “seaward site” hereafter, and (2) 35 km from the ice shelf front, called the “landward site”. In
200 December 2017 and 2018, we revisited and re-measured all stake sites to get annual averaged
201 values of basal melting and strain rates and retrieved the time-series data from the two
202 overwintering stations. Extensive crevassing prevented the three sites closest to the ice rumple
203 (profile B, Fig. 1b) from being revisited in 2018.

204 ApRES uses the frequency-modulated continuous wave (FMCW) technique (Rahman,
205 2016). The instrument transmits a signal sweeping from 200–400 MHz over a period of 1 s to
206 form a chirp (Nicholls et al., 2015). The system has a low-power consumption, with a power to
207 the transmitter antenna of 100 mW. The averaged signal was amplified and de-ramped, a process
208 where the received signal is mixed with a replica of the transmitted signal to extract differences
209 in frequencies. The de-ramped signal was then filtered to amplify the higher frequencies
210 preferentially, which enhanced weaker signals from more distant reflectors. Each sample
211 consisted of 100 chirps, collected over a period of a few minutes. The data were digitized and
212 stored on secure digital cards for further processing.

213 We processed the data following Brennan et al., (2014) and Nicholls et al. (2015)
214 (Supplements Fig. S1). The data were Fourier transformed to give a complex signal amplitude as
215 a function of delay time, or depth, assuming a constant propagation velocity of $168 \text{ m } \mu\text{s}^{-1}$. An
216 amplitude cross correlation between the two returns for a depth range within the firm layer
217 (typically from 40 to 70 m) provided a vertical shift that that approximately accounted for snow
218 accumulation between the visits. The displacement of the reflectors between the two visits were
219 then plotted as a function of depth. To give the necessary depth resolution, the phase of the



220 signals was used to calculate the displacements by cross-correlating 4 m segments of the first
221 profile with the complex conjugate of the corresponding segment of the second. Under the
222 assumption of a constant vertical strain rate between the bottom of the firm layer and just above
223 the ice base, we fit a straight line to the layer displacements. The effect of the correction for
224 snow accumulation between the two visits, both the coarse correction mentioned above and the
225 precise correction inherent in the phase processing, and the effect of the non-linear (with depth)
226 displacements due to firm compaction, are both contained within the intercept at the vertical axis.
227 Thus the basal melt is given by the deviation of the displacement of the basal reflection from the
228 straight line fit (Supplements Fig. S1). The error in the calculated strain was estimated using the
229 quality of fit of the linear regression. The uncertainty in the melt rate was obtained by combining
230 the uncertainty in the strain rate with the uncertainty in the change in the range to the basal
231 reflector, deduced from the signal-to-noise ratios of the two basal reflections.

232 To calculate the hourly time-series data from the two overwintering sites (Fig. 1b), we
233 tracked the basal returns using phase-coherent processing, allowing us to determine the speed of
234 motion of the ice base with respect to the antenna, which hereafter is called the thinning rate. To
235 remove the component of ice-column vertical strain rate caused by tidal variations, we filtered
236 the basal vertical speeds with a 36 h low-pass filter. We removed an annual average vertical
237 strain rate from the filtered basal motion, resulting in net melt rates. We assumed that at periods
238 longer than 36 hours, the variability in strain rate is small compared with the basal melt rate and
239 varies on a much longer timescale than those of interest here.

240 3.2 Low-frequency radar profiling

241 In December 2016, we collected ~180 km of continuous radio-echo sounding profiles
242 across the ice flow (profile A) and along the ice flow (profile B and C) of Nivlisen to measure
243 ice thickness and englacial and basal structure (Fig. 1b). We used a common-offset impulse radar
244 system (Dowdeswell and Evans, 2004) based on the radar developed by Matsuoka et al. (2012)
245 and processing steps following Lindbäck et al. (2014). We used half-wavelength dipole antennas
246 with a 5 MHz centre frequency, with a Kentech impulse transmitter with an average output
247 power of 35 W. The transmitter and receiver systems were mounted on two sleds and towed
248 behind a snowmobile at a speed of $\sim 10 \text{ km h}^{-1}$. We positioned the traces using data from a code-
249 phase global positioning system (GPS) receiver mounted on the radar receiver box 20 m in front



250 of the common mid-point of the antennas along the travelled trajectory of the snowmobile. We
251 post-corrected the height using the Canadian precise point-processing service (CSRS-PPP;
252 Natural Resources Canada, 2017) from a kinematic carrier-phase dual-frequency GPS receiver
253 mounted on the snowmobile. The radar measurements had an average line spacing of ~5 m.

254 Several corrections and filters were applied to the radar data: (1) dewow and bandpass
255 filters, to remove unwanted frequency components in the data, (2) depth-variable gain function,
256 and (3) normal move-out correction to correct for antenna separation, including adjusted travel
257 times for the trigger delay. The basal returns were digitized semi-automatically with a cross-
258 correlation picker at the first break of the bed reflection (Irving et al., 2007). We calculated ice
259 thickness from the picked travel times of the bed return using a constant radio-wave velocity of
260 $168 \text{ m } \mu\text{s}^{-1}$ for ice. We added a correction term of 2 m to account for the faster propagation in
261 the firn based on the snow density (Sect. 3.3). The firn has a depth of ~50 m, derived from the
262 ApRES internal reflectors. Ice draft was calculated from the ice thickness by subtracting the
263 surface elevation, corrected for local sea level (freeboard). We estimated the error in ice
264 thickness by standard analytical error propagation methods (Lapazaran et al., 2016; Taylor,
265 1996), outlined in Lindbäck et al. (2018). The estimation included the error in the radar
266 acquisition and horizontal positioning error, where the radar acquisition errors comprised errors
267 in radio-wave velocity and two-way travel time. Velocity can vary spatially, depending mainly
268 on density. Errors in two-way travel time were estimated to be the range resolution, which is the
269 accuracy of the measurement of the distance between the antenna and the bed. The average radar
270 system error was estimated to $13.3 \pm 1.2 \text{ m}$. The surface and base of the ice shelf is relatively
271 flat, giving very small errors in horizontal positioning ($0.1 \pm 0.2 \text{ m}$). The total error in ice
272 thickness is presented together with the data in Sect. 4.

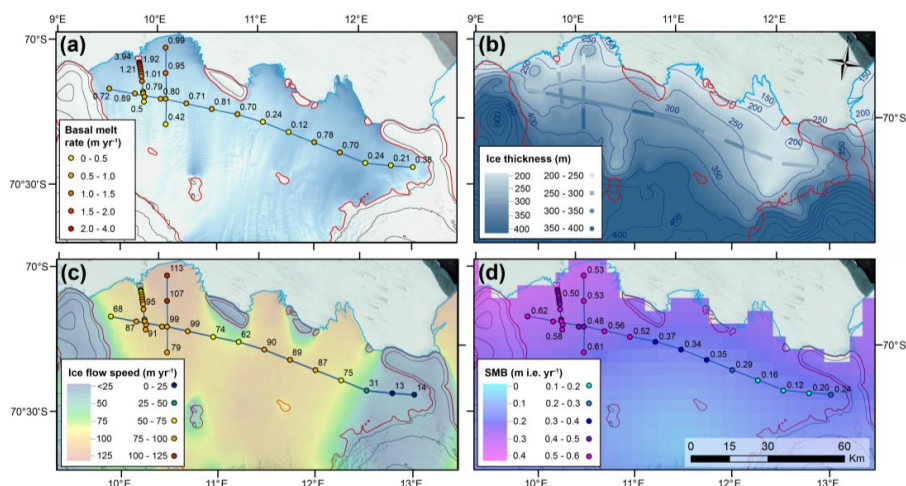
273 3.3 Ice flow and surface mass balance from stakes

274 We measured ice flow and surface mass balance at all 29 ApRES stakes on Nivlisen.
275 Stake height over the surface was measured manually, and stake position was measured statically
276 for 15 minutes using carrier-phase dual-frequency GPS receivers at 1 s logging interval. The
277 stakes were revisited and measured in December 2017 and 2018. We processed the positions
278 using CSRS-PPP. Snow density was measured at five locations on Nivlisen with an auger drill to
279 a depth of 3 m and varied from 430–450 kg m^{-3} . We used the average snow density of 440 kg



280 m^{-3} and an ice density of 917 kg m^{-3} to calculate the surface mass balance in ice equivalent. Ice
281 flow speed and surface mass balance were compared with estimates from satellite data (Rignot et
282 al., 2011) and regional atmospheric modelling (van de Berg et al., 2006).

283



284

285 **Figure 2.** Stake and profile measurements: (a) ApRES-derived annual averaged basal melt rates for 2017 and hill
286 shade (blue) extracted from the Reference Elevation Model of Antarctica (REMA; Howat et al., 2019). See
287 Supplements Fig. S2 for annual averaged basal melt rates for 2018, which is on average within $\pm 10\%$ from the 2017
288 values. (b) Ice thickness from low-frequency radar profiles (point values) and from Bedmap2 product (grid and
289 contour lines; Fretwell et al., 2013). (c) Ice flow speed from stakes and gridded satellite values (Rignot et al., 2011).
290 (d) Surface mass balance (SMB) from stakes and gridded modelled values (Le Brocq et al., 2010). Contour lines and
291 background images are the same as in Fig. 1.

292

293 4 Results

294 In 2017, annual averaged melt rates at 29 stake locations on Nivlisen (Fig. 1b) ranged
295 from 0.12 ± 0.06 to $3.94 \pm 0.04 \text{ m yr}^{-1}$ (Fig. 2a and Fig. 3), with a median value of 0.80 m yr^{-1} .
296 The highest annual averaged melt rates were observed close to an ice rumple at the ice front and
297 the lowest melt rates in the central and eastern parts of the ice shelf. In 2018, annual averaged
298 melt rates at 26 locations, ranged from 0.13 ± 0.06 to $1.48 \pm 0.01 \text{ m yr}^{-1}$, excluding three sites
299 closest to the ice rumple, with high melt rates in 2017 (Supplements Fig. S2). The median melt
300 rate in 2018 was 0.72 m yr^{-1} . Melt rates were slightly lower in the second year at 18 sites and for

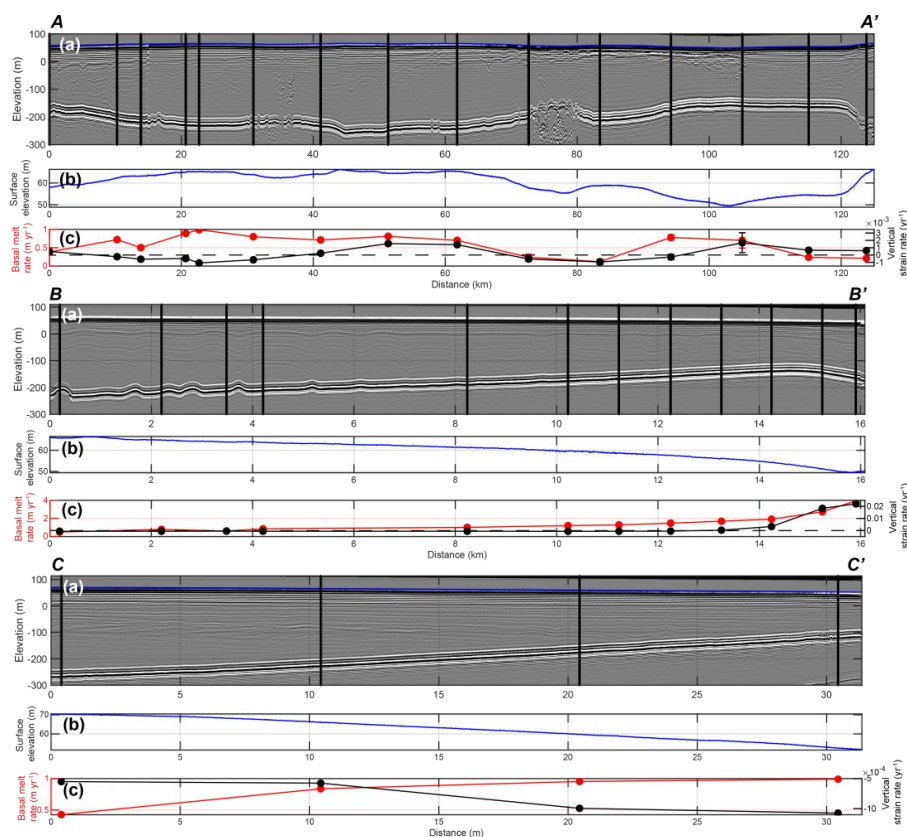


301 8 sites slightly higher. Excluding the three sites closest to the ice rumples in 2017, annual basal
302 melt rates between 2017 and 2018 differ by $\pm 0.1 \text{ m yr}^{-1}$. Errors in melt rates were on average
303 0.023 m yr^{-1} in 2017 and 0.025 m yr^{-1} in 2018.

304 Strain rates were in general low, having a median annual averaged value of -4.7×10^{-4}
305 yr^{-1} in 2017 and $-4.6 \times 10^{-4} \text{ yr}^{-1}$ in 2018. The vertical strain-rate contribution to the average rate
306 of change was on average 22 %. The errors in strain were low, on average $6.2 \times 10^{-5} \text{ yr}^{-1}$ in 2017
307 and $7.1 \times 10^{-5} \text{ yr}^{-1}$ in 2018. For most parts of the ice shelf the strain rates were negative, meaning
308 that the ice was thinning by longitudinal stretching, however, close to the ice rumples mentioned
309 earlier (profile B; Fig. 3) we observed a transition from negative to positive strain rates (from
310 -5.4×10^{-4} to $2.2 \times 10^{-2} \text{ yr}^{-1}$), with increasing compressional thickening of the ice towards the
311 ice rumples. Positive strain rates were also observed for five sites 5–10 km upstream of the larger
312 ice rises in the central and in the eastern part of the ice shelf (profile A; Fig. 3), indicating a far-
313 reaching buttressing effect (distance up to ~ 30 ice thicknesses).

314 The two overwintering ApRES systems were used to derive time series of melt rates. The
315 seaward overwintering site was located 4 km from the ice front and had an ice draft of 130 m,
316 measured with low-frequency radar. It operated for 14 months (from 11 Dec 2016–4 Feb 2017)
317 before the battery failed. Thirty-six hour low-pass filtered melt rates at this site varied from ~ 0 to
318 5.6 m yr^{-1} , where the highest melt rates occurred in summer (29 Jan 2017; Fig. 4a). The
319 landward overwintering site was located 35 km from the ice front and had an ice draft of 280 m.
320 The data cover 23 months (from 4 Jan 2017–27 Nov 2018), except for December 2017 when the
321 instrument was used for measuring annual melt rates at other locations. At this site, 36 h low-
322 pass filtered melt rates varied from ~ 0 to 2.0 m yr^{-1} , where the highest melt rates occurred in
323 winter (12 Jun 2018; Fig. 5a).

324 Ice thickness, measured with low-frequency radar along profiles A, B, and C (Fig. 1b),
325 varied from 160 to 330 m (Fig. 2b), with a median value of 260 m. We observed the thinnest ice
326 close to the ice front along profile C (Fig. 3) and the thickest ice in the southern-most part of the
327 ice shelf along the same profile. The total error in ice thickness along the profiles, including
328 radar system and positioning errors, varied between 10.6 and 15.7 m. The broad thickness pattern
329 agreed with satellite-derived freeboard estimates from Bedmap2 (Fretwell et al., 2013), except



330

331

332 **Figure 3.** Profiles of low-frequency radar, ice surface elevation, basal melt, and strain (locations in Fig. 1b): A–A’
 333 across ice flow from west to east (125 km), B–B’ along ice flow from south to north towards an ice rumple (16 km),
 334 and C–C’ along ice flow from south to north out on an ice tongue (32 km). Sub-panels show (a) radar profiles with
 335 surface elevation (blue line), englacial stratigraphy, and basal elevation (grey tone shading), and locations of ApRES
 336 measurements (black vertical lines), (b) surface elevation from carrier-phase kinematic GPS measurements, and (c)
 337 annual basal melt rate (red) and vertical strain rates (black, dashed = 0) for 2017. Note that the x-axis scales vary
 338 between the three profiles. Surface elevation is referenced to local sea level (freeboard).

339

340 on the western ice tongue (profile C), where the thickness reported in Bedmap2 is too high (Fig.
 341 2b). Ice draft varied from 120 to 280 m with a median value of 220 m (Fig. 3). We observed no
 342 significant relation between basal melting and ice draft. Several locations with undulating
 343 englacial layers, basal channels and crevasses were visible in the radar profiles (Fig. 3). Stake-



344 measured ice flow speeds varied from 13 to 113 m yr⁻¹ in 2017, with an average value of 80 m
345 yr⁻¹, agreeing with satellite estimates (Rignot et al., 2011; Fig. 2c). Surface mass balance values
346 varied between 0.12 and 0.62 m i.e. yr⁻¹ in 2017 with an average of 0.45 i.e. yr⁻¹, higher than the
347 modelled average estimates of 0.2 m i.e. yr⁻¹ (van de Berg et al., 2006), but with the same spatial
348 pattern (Fig. 2d).

349

350 **5 Discussion**

351 In the following sections, we discuss the spatial (Sect. 5.1) and temporal (Sect. 5.2)
352 variations in basal melting and compare our results with other studies from Antarctica. For each
353 section, we also discuss strengths, limitations, and recommendations for future studies.

354 **5.1 Spatial variations in melting**

355 On Nivlisen, we observed the highest annual averaged melt rates (3.9 m yr⁻¹) close to a
356 small (4.2 km²) ice rumple at the ice front (Fig. 2a and Fig. 3). Similar high melt rates (~4 m
357 yr⁻¹) were inferred from satellite data nearby Bawden Ice Rise (Adusumilli et al., 2018). In
358 modelling experiments, the higher melt rates arose from the generation of energetic short-length-
359 scale diurnal topographic vorticity waves (Mueller et al., 2012). This required a thin water
360 column (shallow bathymetry) under the ice-shelf. At Nivlisen, we have no observations of tidal
361 strengths near the ice rumple, but the bathymetry must be shallow since the ice shelf grounds in
362 this region. Ice shelf thinning could potentially increase the water column depth and have a
363 negative (stabilizing) feedback on the melting, reducing the topographic vorticity waves (Mueller
364 et al., 2012, 2018; Padman et al., 2018), though no clear relationship was found between ice draft
365 and basal melting rates in our study. In terms of ice thickness change, the observed thinning from
366 the basal melt is compensated by a positive vertical strain that implies compressional thickening
367 towards the ice rumple (up to 4 m yr⁻¹). Thicker ice towards the ice rumple indicates a
368 buttressing effect on the ice shelf (profile B; Fig. 3). We observed many crevasses in this region
369 that made it, for safety reasons, difficult to revisit the three closest sites during the third field
370 season (Dec 2018). The effects of sustained high melt rates at the Nivlisen ice rumple are
371 uncertain, and modelling work may indicate whether un-grounding of the ice would potentially
372 lead to substantial loss of buttressing (Borstad et al., 2013).



373 Estimates of basal melt rates for Dronning Maud Land ice shelves have mainly used
374 satellite techniques, modelling, or limited spatial or temporal coverage of in situ radar
375 observations (Berger et al., 2017; Langley et al., 2014b). Fimbulisen is situated 400 km west of
376 Nivlisen (Fig. 1a) at the outlet of Jutulstraumen, one of the largest ice streams in Dronning Maud
377 Land. Below the deep keel from Jutulstraumen (300–400 m ice draft), time-averaged melt rates
378 of several meters per year were observed, whereas at the shallower parts of the ice shelf
379 (200–300 m ice draft), lower melt rates were observed (Langley et al., 2014a). In addition,
380 annual-average melt rates were modelled to be near zero for large areas (Hattermann et al.,
381 2014). Hattermann et al. (2014) hypothesized that melt mode 1 occurred at the deepest parts of
382 Fimbulisen (below ice drafts of 400 m). The rising melt plume caused marine accretion at
383 shallower depths closer to the ice front, together with seasonal mode-3 melting, resulting in the
384 low net melt rates, with seasonal marine ice formation being inferred from an ice shelf cavity
385 mooring (Hattermann et al., 2012). Nivlisen is in comparison relatively thin (Fig. 2b) and we
386 have no melt observations from the thicker ice in the southern areas. Grounding line ice drafts
387 (Fig. 1b), derived from Fretwell et al. (2013) and Mouginot et al. (2017), have an average value
388 of 350 m. The deepest part of the grounding line (630 ± 100 m) is located at the outflow of
389 Potsdam Glacier (Fig 1b), where higher melt rates may occur. In addition, Nivlisen has three ice
390 tongues, separated by ice rises and ice rumples, where the ocean can gain access to the inner
391 parts of the ice shelf cavity. At Fimbulisen, Hattermann et al. (2012, 2014) found that a portion
392 of the westward flowing coastal current was diverted under the ice shelf between two ice rises.
393 Similar inflow pathways may also exist beneath the ice tongues of Nivlisen, explaining the
394 variations of melt rates along profile A (Fig. 2a). At Fimbulisen, high melt rates (3 m yr^{-1}) were
395 also observed and modelled close to the ice front at shallow depths (< 200 m; Hattermann et al.,
396 2014; Langley et al., 2014b), which is consistent with our results.

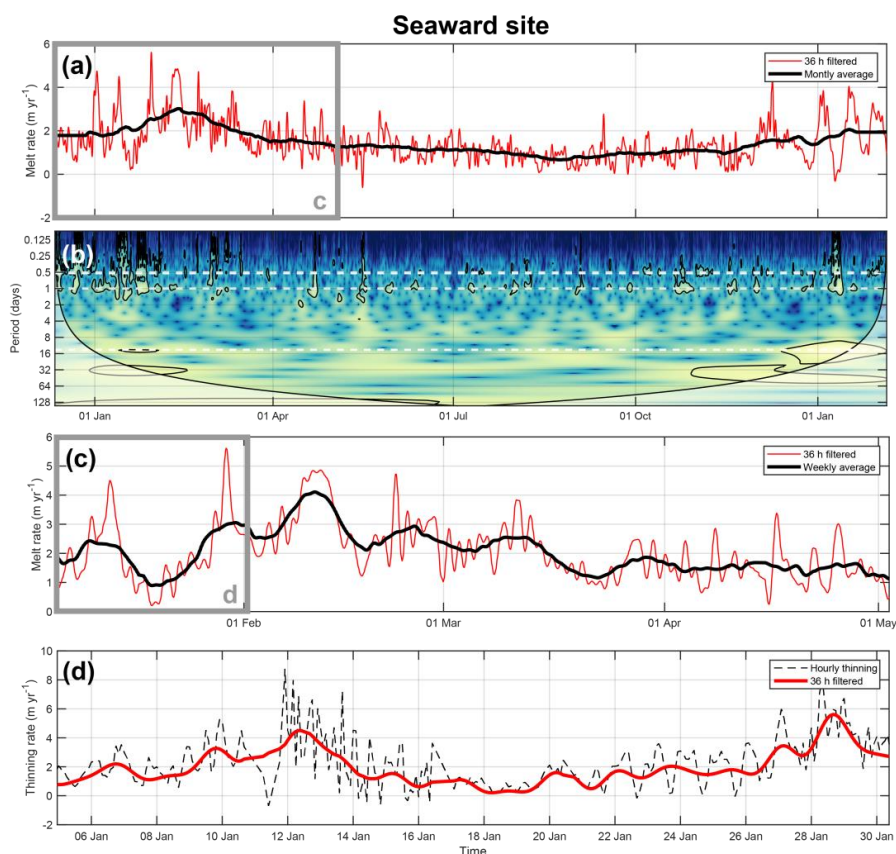
397 In the low-frequency radar profiles, we observed several undulating ice-base features
398 (profile A and B; Fig. 3), where the englacial layers warp downwards, which is likely an
399 indication of basal channels or crevasses. The southernmost measurement in profile B is located
400 at one of these down-warping features, where surface elevation is slightly lowered locally (-0.5
401 m). Higher melt rates were not observed here compared with the surrounding sites, although,
402 higher melt rates typically occur on the flanks of basal channels, rather than at their apex (Berger



403 et al., 2017). The channel may have formed at an upstream ice rumple and been passively
404 advected downstream (Fig. 2a). Basal channels are important features influencing the ice-shelf
405 stability, since they affect ice-shelf cavity circulation and play a role in the exchange of heat and
406 mass between the ocean and ice shelf (Gladish et al., 2012; McGrath et al., 2012; Millgate et al.,
407 2013; Stanton et al., 2013). Basal channels are not restricted to rapidly melting ice shelves and
408 have been observed elsewhere in Dronning Maud Land, at Fimbulisen (Langley et al., 2014a)
409 and Roi Baudouin Ice Shelf (Fig. 1a; Berger et al., 2017). Detailed studies of these features
410 together with basal melting are needed to understand their initiation, evolution, and role in the
411 overall mass balance of ice shelves (Alley et al., 2016).

412 5.2 Temporal variations in melting

413 Melt rates at Nivlisen varied on a broad range of timescales (Fig. 4 and 5). At the
414 seaward site, we observed a seasonal signal, where the monthly averaged melt rates were two to
415 three times higher in the summer than in winter (Fig. 4a, Supplements Fig. S3). At the landward
416 site, we observed no seasonal pattern, however, some variability on monthly time-scales was
417 present (Fig. 5a, Supplements Fig. S3). We performed a continuous wavelet transform on the
418 time-series data from the two overwintering sites, based on the method and software package
419 provided by Grinsted et al. (2004). The wavelet transform is used to study localized intermittent
420 periodicities, in contrast to more traditional mathematical methods, such as Fourier analysis,
421 which assumes that the underlying process is stationary in time. We used a Morlet wavelet with
422 $\omega_0 = 6$, which provides a good balance between time and frequency localization. The wavelet
423 transform shows the normalized thinning rates at different scales to identify dominant periods of
424 variability in time (Fig. 4b, 5b). The statistical significance was assessed relative to the null
425 hypothesis, modelled by a first order autoregressive process. The wavelet transform has edge
426 artefacts since it is not completely localized in time, as indicated by the cone of influence,
427 masking out low frequency signals at the beginning and end of the time series. The thinning
428 variability at diurnal timescales, and to some extent semi-diurnal timescales, varied at an
429 approximately two-weekly period. This reflects the fortnightly spring-neap tidal cycle at which
430 the strength of the tidal currents varies due to the interference of different constituents, usually
431 M_2 and S_2 in this area (plotted as white dashed lines in Fig. 4b and 5b). Stronger tidal currents
432 increase the heat exchange at the ice-ocean interface and may hence cause more rapid melt. At

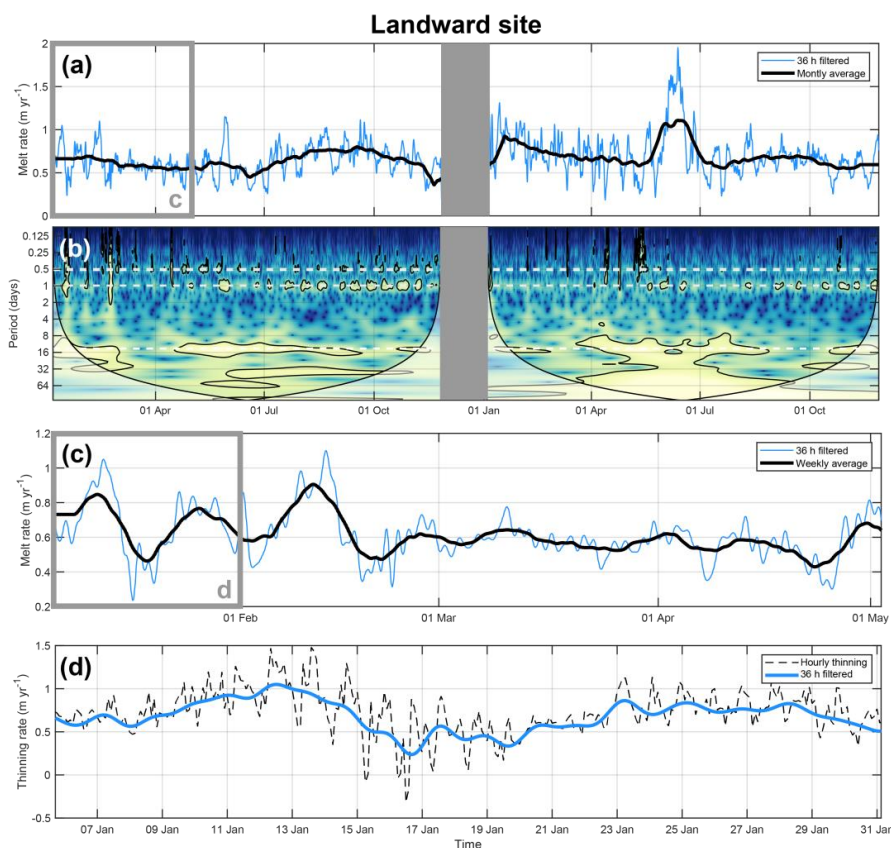


433

434 **Figure 4.** Basal melt and thinning rates for the seaward overwintering site, with variations on time scales of (a)
 435 months (11 Dec 2016–4 Feb 2017), (c) weeks (1 Jan–1 May 2017), and (d) days (1–31 Jan 2017). Dashed black line
 436 in (d) is the unfiltered raw data with thickness change including strain rates. (b) Continuous wavelet transform of the
 437 normalized thinning to identify the dominant modes of variability at different time scales. The left axis is the Fourier
 438 period. The colour shading represents the thinning associated with fluctuations over the course of the year with a
 439 particular time period (yellow = high power, blue = low power). The black contours delimit significant modes of
 440 variance at 95 % against red noise. Within the cone of influence, shown as a lighter shade, edge effects become
 441 important. Dashed white lines show the periods of major tidal constituents ($0.5 \text{ d} \approx K_1$, $1 \text{ d} \approx M_2/S_2$, and $14 \text{ d} \approx M_f$).

442

443 periods shorter than 36 hours, however, we cannot differentiate the strain signal from the melt
 444 signal. We also see some evidence of a slower variability in data centred on 2–4 days (Fig. 4d
 445 and 5d), which may be a result of mesoscale activity passing by the site (eddies or internal
 446 waves), which then show up in the melt rate. This is to some extent supported by Fourier



447
 448 **Figure 5.** Basal melt and thinning rates for the landward overwintering site, with variations on time scales of (a)
 449 months (4 Jan 2017–27 Nov 2018), (c) weeks (4 Jan–1 May 2017), and (d) days (4–31 Jan 2017). (b) Continuous
 450 wavelet transform as described in Fig. 4. Grey box masks a time period with no data. All legends are the same as
 451 Fig. 4.

452
 453 analysis of the normalized 36 h filtered melt rates, which show peaks in power spectral density at
 454 2–4 days, mostly visible at the seaward site (Supplements Fig. S4).

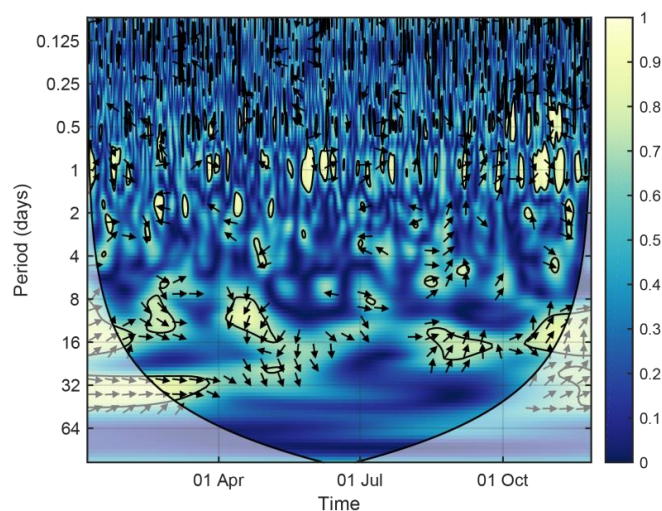
455 At the landward site, we observed no increased melting in summer, but we observed one
 456 melt peak in winter (12 June 2018; Fig. 5a). The melt event may have been caused by pulses of
 457 modified warm deep water reaching the base of the ice shelf as described by Hattermann et al.
 458 (2012), but it could also relate to other mesoscale activities within the cavity. In any case, the
 459 isolated event and the generally low melt rates suggest that warm deep water had limited access



460 to the base of Nivlisen during 2017 and 2018. The observation is consistent with earlier studies,
461 showing that ice shelf cavities in this region are mainly filled with cold and fresh eastern shelf
462 water (Nicholls et al., 2006; Thompson et al., 2018). Along most of the Dronning Maud Land
463 coast, the ice shelf cavities are separated from warm deep water by the Antarctic slope front,
464 which is a pronounced transition zone over the narrow continental shelf between eastern shelf
465 water and warm deep water, mainly attributed to coastal downwelling caused by the prevailing
466 easterly winds (Sverdrup, 1954; Thompson et al., 2018). Many factors control the extent to
467 which warm deep water can access the ice shelf cavities, such as the stability of the Antarctic
468 slope front, local circulation, and bathymetry. The coastal dynamics that set the warm deep water
469 depth along the continental shelf break involves the balance between wind-driven Ekman
470 overturning and counteracting eddy fluxes (Nøst et al., 2011; Thompson et al., 2014). These
471 processes respond to changes in wind and buoyancy fluxes (Hattermann et al., 2014; Stewart and
472 Thompson, 2016), including self-amplifying feedback of increased fresh water input from
473 increased basal melting (Hattermann, 2018).

474 We studied the coherency between the two overwintering melt sites in a wavelet
475 coherence (Grinsted et al., 2004) for the overlapping time periods in 2017 (Fig. 6). The wavelet
476 coherence analysis finds significant coherence even if the common power is low, and it shows
477 significant confidence levels against red noise backgrounds. Locally phase-locked behaviour can
478 also be revealed; at weekly to monthly periods (7 to 30 days) in summer to fall (Jan–Apr 2017)
479 the melt rates were in phase, whereas in winter (Apr–Jun) the melting at the seaward site led the
480 increased signal, preceding the melt at the landward site. In late winter (Sept), the phase shifted
481 to the landward site leading the melt. At Fimbulisen, the inflow of summer-warmed Antarctic
482 surface water was observed at moorings close to the ice shelf front with a clear seasonal signal in
483 water temperatures and salinity (Hattermann et al., 2012). Hattermann et al. (2014) suggested
484 that Antarctic surface water can reside for several months in the ice shelf cavity, after initially
485 being subducted beneath the ice front, potentially affecting basal melting deep inside the cavity.
486 The observed melt rate pattern beneath Nivlisen may be an indication of similar movement of
487 water masses below the ice shelf and further modelling is needed to study these processes,
488 currently being hampered by the lack of knowledge of bottom topography beneath the ice shelf.

489



490

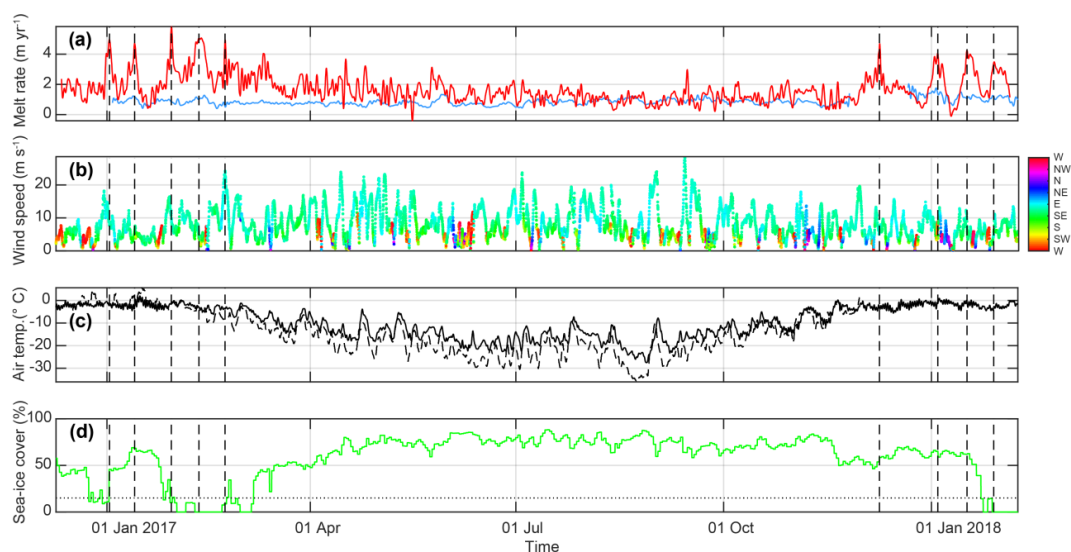
491 **Figure 6.** Wavelet coherence between the seaward and landward site (4 Jan–27 Nov 2017), showing times where
492 the melt rates have common power. The phase relationship is shown as arrows. At longer periods (8–30 days) in
493 summer to fall (Jan–Apr) the signals are in phase (arrows pointing right), whereas in winter (Apr–Jun) the melt at
494 the seaward site leads the signal (arrows pointing down). In late winter (Sept) the phase shifts to the landward site
495 leading the signal (arrows pointing up).

496

497 We compared the basal melt rates with atmospheric ERA5 reanalysis data of wind speed,
498 wind direction, sea-ice cover, air pressure, and temperature (Fig. 7) produced by the European
499 Centre for Medium-Range Weather Forecasts (Copernicus Climate Change Service (C3S), 2017)
500 at a grid point 10 km north of the ice shelf front (Fig. 1b). ERA5 wind speeds at Nivlisen varied
501 on daily timescales, ranging from 0 to 28 m s⁻¹. Winds generally blew from the east (Fig. 7b),
502 corresponding to the pressure gradients imposed by the cyclonic system that dominates the
503 Weddell Sea. Wind forcing can play an important role in downwelling and transportation of
504 summer-warmed Antarctic surface water into the ice-shelf cavity (Zhou et al., 2014). We
505 calculated the coherence between the normalized melt rates at the seaward site and wind speeds.
506 The statistical significance level was estimated using Monte Carlo simulation with a Fourier
507 transform method, where a large set of surrogate data set pairs were generated using phase
508 randomization (Schreiber and Schmitz, 2000). In summer, we find a significant coherence
509 between melt rates and wind speeds ($r = 0.36$, $p < 0.05$; Supplements Fig. S5). Inspecting
510 individual melt peaks in the summer (dashed vertical lines in Fig. 7) show that they coincide



511 with higher wind events, and have a time lag of ~ 0 to 3 days. We found no such coherence in
512 winter. The variability in winter may be due to the transport mainly dominated by eddies, shed
513 by instabilities in the along-slope current. Sea-ice cover according to ERA5 decreased or was
514 absent (defined as less than 15 %) during summer and fall (January to March; Fig. 7c), also
515 coinciding with higher melt rates. When melt increased in early summer at the seaward site (Dec
516 2016 and 2017; Fig 4a), we observed less sea-ice cover close to the ice shelf front, which is the
517 time when solar radiation may warm the surface waters. Satellite images also show the
518 variability in sea ice (Supplements Fig. S6), with open water east of the ice tongue in December
519 2017 that is not resolved in detail in the ERA5 sea-ice cover. The ERA5 air temperatures at 2 m
520 varied mostly on seasonal time scales, with temperatures between 0 and -10°C in summer, and
521 down to -24°C in winter (Fig. 7d). The temperature variability in the reanalysis data on shorter
522 timescales agreed with our weather station on Leningradkollen ice rise (190 m a.s.l.), however,
523 the seasonal temperature signal had a lower amplitude than at the weather station, which
524 measured temperatures down to -38°C .



525
526 **Figure 7.** Melt peaks compared with atmospheric forcing and sea ice: (a) Thirty-six hour low-pass filtered basal
527 melt rates at seaward site (red) and landward site (blue). ERA5 reanalysis surface data of (b) wind speed and
528 direction, (c) 2 m air temperature, where dashed black line is data from a weather station (Fig. 1b), and (d) sea-ice
529 cover, where the dotted line is 15 % (definition of no sea ice). Periods with pronounced basal melting are indicated
530 with vertical dashed lines for easier comparison.



531 In summary, the observed higher melt rates during summer and fall correlate with higher
532 wind speeds, when there is less sea-ice cover and higher air temperatures. We hypothesize that
533 summer-warmed Antarctic surface water was pushed by wind under the ice shelf at the front.
534 Warming of the surface water is projected to increase ice-shelf melting along Dronning Maud
535 Land in future climate scenarios (Kusahara and Hasumi, 2013) and recent studies suggest that
536 non-linear feedbacks may facilitate an irreversible transition into a state of high melting in the
537 Weddell Sea (Hattermann, 2018; Hellmer et al., 2017). Surface winds are projected to intensify
538 over the next century with increased greenhouse gas emissions (Greene et al., 2017) and extreme
539 changes in sea-ice extent have occurred in recent years (Shepherd et al., 2018). Natural
540 variability in the atmosphere and oceans remains poorly understood (Turner et al., 2016) and the
541 declining extent of ice shelves around Antarctica has been ascribed to a complex set of processes
542 linking the atmosphere, ocean, and sea ice (Adusumilli et al., 2018; Greene et al., 2017).
543
544

545 **6 Conclusions**

546 We present a two year record of basal melting at Nivlisen, in Dronning Maud Land, East
547 Antarctica, at high spatial and temporal resolution using in situ phase-sensitive radar
548 measurements. Annual averaged melt rates are in general moderate, but high melt rates were
549 observed close to a grounded feature near the ice shelf front. Daily measurements also reveal a
550 seasonal melt pattern close to the ice shelf front, where the highest melt rates occurred in
551 summer. Comparing the seasonality in basal melting with forcing from atmospheric reanalysis
552 data, we found that the variability in the basal melt is likely caused by summer-warmed surface
553 water pushed by the wind into the ice-shelf cavity. Farther into the ice-shelf cavity, we observe a
554 different melt regime, with significantly lower melt rates and a clearer tidal signal. We conclude
555 that warm deep ocean water has a limited effect on the basal melting of Nivlisen, likely because
556 the present configuration of the Antarctic slope front, which separates the deeper water from the
557 continent, protects the ice shelf from those warmer water masses.

558 Our study highlights that, although many of the ice shelves of East Antarctica have
559 generally low melt rates, their seaward portions remain susceptible to higher rates of melting due
560 to the influence of summer-warmed surface waters. Reduced sea-ice cover and higher wind



561 speeds may increase leading mode-3 melting, while weaker winds and/or changes in the surface
562 buoyancy forcing may increase exposure of the sub ice-shelf cavities to warm deep water and
563 therefore increase mode-2 melting. Increases in basal melting will tend to thin the ice shelves and
564 reduce the buttressing on the inland ice sheet. Many ice shelves like Nivlisen are stabilized by
565 pinning points at their ice fronts, which may be sensitive areas for future change. It remains to be
566 understood to what extent, increased summer-warmth driven melting, intensified in the vicinity
567 of these pinning points may affect the ice flow dynamics and ice-shelf stability. Our study shows
568 the use of and need for continuous in situ monitoring of Antarctic ice shelves to resolve
569 variability in basal melting that is not captured in satellite data. Long-term, high-resolution time-
570 series data are important to understand the complex mechanisms involved in ice shelf–ocean
571 interactions, which in turn is important for ice sheet models.

572

573 **Data availability**

574 The compiled data sets of basal melt, strain rates, ice speeds, surface mass balance, and low-
575 frequency radar profiles will be available at the Norwegian Polar Data Centre
576 (<https://data.npolar.no>).

577

578 **Author contribution**

579 KL led the overall data analysis and interpretations, and prepared the paper with contributions
580 from all co-authors. KL, GM, and BP collected the ApRES, ice speed and surface mass balance
581 in the field. KWN was responsible for the ApRES system setup. KM was responsible for the
582 low-frequency radar system and collected the data in field. TH contributed to the discussion
583 section. MT and KM were the project leaders.

584

585 **Competing interests**

586 KM is a member of the editorial board of the journal.

587



588 **Acknowledgments**

589 This work was part of the MADICE (Mass balance, dynamics, and climate of the central
590 Dronning Maud Land coast, East Antarctica) project, funded by the Research Council of Norway
591 (project 248780) and the Ministry of Earth Sciences, India (project MoES/Indo-Nor/PS-3/2015).
592 Logistic support was provided from Indian Maitri Station and Norwegian Troll Station,
593 Antarctica; we would like to thank the NCPOR and NPI logistic heads and personnel who helped
594 us in the field. We would also like to thank Chris Borstad for estimating flowlines to the rumple,
595 Harvey Goodwin for assessing field safety, Vikram Goel for helping collect the data in field, and
596 Robert Graham for providing the ERA5 data. Figures 1 and 2 were prepared using Quantarctica
597 (quantarctica.npolar.no). For the REMA data set we acknowledge the following: DEMs provided
598 by the Byrd Polar and Climate Research Center and the Polar Geospatial Center under NSF-OPP
599 awards 1543501, 1810976, 1542736, 1559691, 1043681, 1541332, 0753663, 1548562, 1238993
600 and NASA award NNX10AN61G. Computer time provided through a Blue Waters Innovation
601 Initiative. DEMs produced using data from DigitalGlobe, Inc.

602

603 **References**

604 Adusumilli, S., Fricker, H. A., Siegfried, M. R., Padman, L., Paolo, F. S. and Ligtenberg,
605 S. R. M.: Variable Basal Melt Rates of Antarctic Peninsula Ice Shelves, 1994–2016, *Geophys.*
606 *Res. Lett.*, 45, 4086–4095, doi:10.1002/2017GL076652, 2018.

607 Alley, K. E., Scambos, T. A., Siegfried, M. R. and Fricker, H. A.: Impacts of warm water
608 on Antarctic ice shelf stability through basal channel formation, *Nat. Geosci.*, 9, 290, 2016.

609 De Angelis, H. and Skvarca, P.: Glacier Surge After Ice Shelf Collapse, *Science*, 299,
610 1560–1563, 2003.

611 Anshütz, H., Eisen, O., Oerter, H., Steinhage, D. and Scheinert, M.: Investigating small-
612 scale variations of the recent accumulation rate in coastal Dronning Maud Land, East Antarctica,
613 *Ann. Glaciol.*, 46, 14–21, 2007.

614 Arndt, J. E., Schenke, H. W., Jakobsson, M., Nitsche, F. O., Buys, G., Goleby, B.,
615 Rebesco, M., Bohoyo, F., Hong, J., Black, J., Greku, R., Udintsev, G. and Barrios, F.: The



- 616 International Bathymetric Chart of the Southern Ocean (IBCSO) Version 1.0 — A new
617 bathymetric compilation covering circum-Antarctic waters, *Geophys. Res. Lett.*, 40, 3111–3117,
618 doi:10.1002/grl.50413, 2013.
- 619 Bamber, J. L., Westaway, R. M., Marzeion, B. and Wouters, B.: The land ice contribution
620 to sea level during the satellite era, *Environ. Res. Lett.*, 13, 2018.
- 621 van de Berg, W. J., van den Broeke, M. R., Reijmer, C. H. and van Meijgaard, E.:
622 Reassessment of the Antarctic surface mass balance using calibrated output of a regional
623 atmospheric climate model, *J. Geophys. Res.*, 111, 1–15, doi:10.1029/2005JD006495, 2006.
- 624 Berger, S., Drews, R., Helm, V., Sun, S. and Pattyn, F.: Detecting high spatial variability
625 of ice-shelf basal mass balance, Roi Baudouin Ice Shelf, Antarctica, *Cryosph.*, 11, 2675–2690,
626 doi:10.5194/tc-2017-41, 2017.
- 627 Bindschadler, R., Vornberger, P., Fleming, A., Fox, A., Mullins, J., Binnie, D., Jean, S.,
628 Granneman, B. and Gorodetzky, D.: Remote Sensing of Environment The Landsat Image Mosaic
629 of Antarctica, *Remote Sens. Environ.*, 112(12), 4214–4226, doi:10.1016/j.rse.2008.07.006, 2008.
- 630 Borstad, C. P., Rignot, E., Mouginot, J. and Schodlok, M. P.: Creep deformation and
631 buttressing capacity of damaged ice shelves : theory and application to Larsen C ice shelf,
632 *Cryosph.*, 7, 1931–1947, doi:10.5194/tc-7-1931-2013, 2013.
- 633 Brennan, P. V., Lok, L. B., Nicholls, K. and Corr, H.: Phase-sensitive FMCW radar
634 system for high-precision Antarctic ice shelf profile monitoring, *IET Radar Sonar Navig.*, 8(7),
635 776–786, doi:10.1049/iet-rsn.2013.0053, 2014.
- 636 British Antarctic Survey: Instrument: Phase-sensitive radar (ApRES), Filchner Ice Shelf,
637 [online] Available from: [https://www.bas.ac.uk/polar-operations/sites-and-](https://www.bas.ac.uk/polar-operations/sites-and-facilities/facility/phase-sensitive-radar-apres/)
638 [facilities/facility/phase-sensitive-radar-apres/](https://www.bas.ac.uk/polar-operations/sites-and-facilities/facility/phase-sensitive-radar-apres/) (Accessed 13 November 2018), 2018.
- 639 Le Brocq, A. M., Payne, A. J. and Vieli, A.: An improved Antarctic dataset for high
640 resolution numerical ice sheet models (ALBMAP v1), *Earth Syst. Sci. Data*, 2(2), 247–260,
641 doi:10.5194/essd-2-247-2010, 2010.
- 642 Copernicus Climate Change Service (C3S): ERA5: Fifth generation of ECMWF
643 atmospheric reanalyses of the global climate, Copernicus Clim. Chang. Serv. Clim. Data Store



- 644 [online] Available from: <https://www.ecmwf.int/en/forecasts/datasets/reanalysis-datasets/era5>
645 (Accessed 1 November 2018), 2017.
- 646 Corr, H. F. J., Jenkins, A., Nicholls, K. W. and Doake, C. S. M.: Precise measurement of
647 changes in ice-shelf thickness by phase-sensitive radar to determine basal melt rates, *Geophys.*
648 *Res. Lett.*, 29(8), 1–4, 2002.
- 649 Dareluis, E. and Sallée, J. B.: Seasonal Outflow of Ice Shelf Water Across the Front of
650 the Filchner Ice Shelf, Weddell Sea, Antarctica, *Geophys. Res. Lett.*, 45, 3577–3585,
651 doi:10.1002/2017GL076320, 2017.
- 652 Davis, P. E. D., Jenkins, A., Nicholls, K. W., Brennan, P. V., Povl, E., Heywood, K. J.,
653 Dutrioux, P., Cho, K. and Wan, T.: Variability in Basal Melting Beneath Pine Island Ice Shelf on
654 Weekly to Monthly Timescales, *J. Geophys. Res. Ocean.*, doi:10.1029/2018JC014464, 2018.
- 655 Depoorter, M. A., Bamber, J. L., Griggs, J. A., Lenaerts, J. T. M., Ligtenberg, S. R. M.,
656 Broeke, M. R. Van Den and Moholdt, G.: Calving fluxes and basal melt rates of Antarctic ice
657 shelves, *Nature*, 502(7469), 89–92, doi:10.1038/nature12567, 2013.
- 658 Dong, J., Speer, K. and Jullion, L.: The Antarctic Slope Current near 30 deg E, *J.*
659 *Geophys. Res. Ocean.*, 121, 1051–1062, 2016.
- 660 Dowdeswell, J. A. and Evans, S.: Investigations of the form and flow of ice sheets and
661 glaciers using radio-echo sounding, *Reports Prog. Phys.*, 67(10), 1821–1861, doi:10.1088/0034-
662 4885/67/10/R03, 2004.
- 663 Dupont, T. K. and Alley, R. B.: Assessment of the importance of ice-shelf buttressing to
664 ice-sheet flow, *Geophys. Res. Lett.*, 32, 1–4, doi:10.1029/2004GL022024, 2005.
- 665 Favier, L., Gagliardini, O., Durand, G. and Zwinger, T.: A three-dimensional full Stokes
666 model of the grounding line dynamics: effect of a pinning point beneath the ice shelf, *Cryosph.*
667 *Cryosph.*, 6, 101–112, doi:10.5194/tc-6-101-2012, 2012.
- 668 Fretwell, P., Pritchard, H. D., Vaughan, D. G., Bamber, J. L., Barrand, N. E., Bell, R.,
669 Bianchi, C., Bingham, R. G., Blankenship, D. D., Casassa, G., Catania, G., Callens, D., Conway,
670 H., Cook, A. J., Corr, H. F. J., Damaske, D., Damm, V., Ferraccioli, F., Forsberg, R., Fujita, S.,
671 Gim, Y., Gogineni, P., Griggs, J. A., Hindmarsh, R. C. A., Holmlund, P., Holt, J. W., Jacobel, R.



- 672 W., Jenkins, A., Jokat, W., Jordan, T., King, E. C., Kohler, J., Krabill, W., Riger-Kusk, M.,
673 Langley, K. A., Leitchenkov, G., Leuschen, C., Luyendyk, B. P., Matsuoka, K., Mougnot, J.,
674 Nitsche, F. O., Nogi, Y., Nost, O. A., Popov, S. V., Rignot, E., Rippin, D. M., Rivera, A.,
675 Roberts, J., Ross, N., Siegert, M. J., Smith, A. M., Steinhage, D., Studinger, M., Sun, B., Tinto,
676 B. K., Welch, B. C., Wilson, D., Young, D. A., Xiangbin, C. and Zirizzotti, A.: Bedmap2:
677 improved ice bed, surface and thickness datasets for Antarctica, *Cryosph.*, 7(1), 375–393,
678 doi:10.5194/tc-7-375-2013, 2013.
- 679 Gille, S. T.: Warming of the Southern Ocean Since the 1950s, *Science*, 295, 1275–1278,
680 2002.
- 681 Gingele, F. X., Kuhn, G., Maus, B., Melles, M. and Schöne, T.: Holocene ice retreat from
682 the Lazarev Sea shelf, East Antarctica, *Cont. Shelf Res.*, 17(2), 137–163, 1997.
- 683 Gladish, C. V., Holland, D. M., Holland, P. R. and Price, S. F.: Ice-shelf basal channels in
684 a coupled ice/ocean model, *J. Glaciol.*, 58(212), 1227–1244, doi:10.3189/2012JoG12J003, 2012.
- 685 Gladstone, R. M., Lee, V., Rougier, J., Payne, A. J., Hellmer, H., Le, A., Shepherd, A.,
686 Edwards, T. L., Gregory, J. and Cornford, S. L.: Calibrated prediction of Pine Island Glacier
687 retreat during the 21st and 22nd centuries with a coupled flowline model, *Earth Planet. Sci. Lett.*,
688 333–334, 191–199, doi:10.1016/j.epsl.2012.04.022, 2012.
- 689 Greene, C. A., Blankenship, D. D., Gwyther, D. E., Silvano, A. and Wijk, E. Van: Wind
690 causes Totten Ice Shelf melt and acceleration, *Sci. Adv.*, 3, 1–5, doi:10.3934/mbe.2012.9.125,
691 2017.
- 692 Grinsted, A., Moore, J. C. and Jevrejeva, S.: Application of the cross wavelet transform
693 and wavelet coherence to geophysical time series, *Nonlinear Process. Geophys.*, 11(5/6), 561–
694 566, doi:10.5194/npg-11-561-2004, 2004.
- 695 Hattermann, T.: Antarctic Thermocline Dynamics along a Narrow Shelf with Easterly
696 Winds, *J. Phys. Oceanogr.*, 48, 2419–2442, doi:10.1175/JPO-D-18-0064.1, 2018.
- 697 Hattermann, T., Nøst, O. A., Lilly, J. M. and Smedsrud, L. H.: Two years of oceanic
698 observations below the Fimbul Ice Shelf, Antarctica, *Geophys. Res. Lett.*, 39(L12605),
699 doi:10.1029/2012GL051012, 2012.



- 700 Hattermann, T., Smedsrud, L. H., Nøst, O. A., Lilly, J. M. and Galton-fenzi, B. K.: Eddy-
701 resolving simulations of the Fimbul Ice Shelf cavity circulation: Basal melting and exchange
702 with open ocean, *Ocean Model.*, 82, 28–44, doi:10.1016/j.ocemod.2014.07.004, 2014.
- 703 Hazel, J. E. and Stewart, A. L.: Are the Near-Antarctic Easterly Winds Weakening in
704 Response to Enhancement of the Southern Annular Mode?, *J. Clim.*, 32(6), 1895–1918,
705 doi:10.1175/jcli-d-18-0402.1, 2019.
- 706 Hellmer, H. ., Kauker, F., Timmermann, R. and Hattermann, T.: The Fate of the Southern
707 Weddell Sea Continental Shelf in a Warming Climate, *J. Clim.*, 30, 4337–4350,
708 doi:10.1175/JCLI-D-16-0420.1, 2017.
- 709 Heywood, K. J., Locarnini, R. A., Frew, R. D., Dennis, P. F. and King, B. A.: Transport
710 and water masses of the Antarctic slope front system in the eastern Weddell Sea, *Ocean. Ice,*
711 *Atmos. Interact. Antarct. Cont. Margin*, 24(January), 203–214, doi:10.1029/ar075p0203, 1998.
- 712 Hogg, A. E. and Gudmundsson, G. H.: Impacts of the Larsen-C Ice Shelf calving event,
713 *Nat. Clim. Chang.*, 7, 540–542, doi:10.1038/nclimate3359, 2017.
- 714 Holland, P. R., Brisbourne, A., Corr, H. F. J., McGrath, D., Purdon, K., Paden, J.,
715 Fricker, H. A., Paolo, F. S. and Fleming, A. H.: Oceanic and atmospheric forcing of Larsen C
716 Ice-Shelf thinning, *Cryosph.*, 9(3), 1005–1024, doi:10.5194/tc-9-1005-2015, 2015.
- 717 Horwath, M., Dietrich, R., Baessler, M., Nixdorf, U., Steinhage, D., Fritzsche, D.,
718 Damm, V. and Reitmayr, G.: Nivlisen, an Antarctic ice shelf in Dronning Maud Land: geodetic –
719 glaciological results from a combined analysis of ice thickness, ice surface height and ice-flow
720 observations, *J. Glaciol.*, 52(176), 17–30, 2006.
- 721 Howat, I. M., Porter, C., Smith, B. E., Noh, M. J. and Morin, P.: The Reference Elevation
722 Model of Antarctica, *Cryosph.*, 13, 665–674, doi:10.5194/tc-13-665-2019, 2019.
- 723 Irving, J. D., Knoll, M. D. and Knight, R. J.: Improving crosshole radar velocity
724 tomograms: A new approach to incorporating high-angle travelttime data, *Geophysics*, 72(4), 31–
725 41, doi:10.1190/1.2742813, 2007.
- 726 Jacobs, S. S., Helmer, H. H., Doake, C. S. M., A, J. and Frolich, R. M.: Melting of ice
727 shelves and the mass balance of Antarctica, *J. Glaciol.*, 38(130), 375–387, 1992.



- 728 Jenkins, A. and Doake, C. S. M.: Ice-ocean interaction on Ronne Ice Shelf, Antarctica, J.
729 Geophys. Res. Ocean., 96(C1), 791–813, doi:10.1029/90JC01952, 1991.
- 730 Jenkins, A., Corr, H. F. J., Nicholls, K. W., Stewart, C. L. and Doake, C. S. M.:
731 Interactions between ice and ocean observed with phase-sensitive radar near an Antarctic ice-
732 shelf grounding line, J. Glaciol., 52(178), 325–346, 2006.
- 733 Jenkins, A., Dutrieux, P., Jacobs, S. S., McPhail, S. D., Perrett, J. R., Webb, A. T. and
734 White, D.: Observations beneath Pine Island Glacier in West Antarctica and implications for its
735 retreat, Nat. Geosci., 3, 468, 2010.
- 736 Joughin, I. and Vaughan, D. G.: Marine ice beneath the Filchner-Ronne Ice Shelf,
737 Antarctica: a comparison of estimated thickness distributions, Ann. Glaciol., 39, 511–517, 2004.
- 738 Joughin, I., Smith, B. E. and Medley, B.: Marine Ice Sheet Collapse Potentially Under
739 Way for the Thwaites Glacier Basin, West Antarctica, Science, 344, 735–739, 2014.
- 740 Kingslake, J., Ng, F. and Sole, A.: Modelling channelized surface drainage of
741 supraglacial lakes, J. Glaciol., 61(225), 185–199, doi:10.3189/2015JG14J158, 2015.
- 742 Kusahara, K. and Hasumi, H.: Modeling Antarctic ice shelf responses to future climate
743 changes and impacts on the ocean Ž, J. Geophys. Res. Ocean., 118, 2454–2475,
744 doi:10.1002/jgrc.20166, 2013.
- 745 Kwok, R. and Comiso, J.: Southern Ocean Climate and Sea Ice Anomalies Associated
746 with the Southern Oscillation, J. Clim., 15, 487–501, 2002.
- 747 Kwok, R., Comiso, J. C., Lee, T. and Holland, P. R.: Linked trends in the South Pacific
748 sea ice edge and Southern Oscillation Index, J. Geophys. Res., 43, 295–302,
749 doi:10.1002/2016GL070655.Received, 2016.
- 750 Langley, K., von Deschanden, A., Kohler, J., Sinisalo, A., Matsuoka, K., Hattermann,
751 T., Humbert, A., Nøst, O. A. and Isaksson, E.: Complex network of channels beneath an
752 Antarctic ice shelf, Geophys. Res. Lett., 41, 1209–1215, 2014a.
- 753 Langley, K., Kohler, J., Sinisalo, A., Øyan, M. J., Hamran, S. E., Hattermann, T.,
754 Matsuoka, K., Nøst, O. A. and Isaksson, E.: Low melt rates with seasonal variability at the base
755 of Fimbul Ice Shelf, East Antarctica, revealed by in situ interferometric radar measurements,



- 756 Geophys. Res. Lett., 41(22), 8138–8146, doi:10.1002/2014GL061782, 2014b.
- 757 Lapazaran, J. J., Otero, J. and Navarro, F. J.: On the errors involved in ice-thickness
758 estimates I: ground- penetrating radar measurement errors, *J. Glaciol.*, 1–13,
759 doi:10.1017/jog.2016.93, 2016.
- 760 Lenaerts, J. T. M., Brown, J., Broeke, M. R. V. A. N. D. E. N., Matsuoka, K., Drews, R.,
761 Callens, D., Philippe, M., Gorodetskaya, I. V, Meijgaard, E. V. A. N., Reijmer, C. H., Pattyn, F.
762 and Lipzig, N. P. M. V. A. N.: High variability of climate and surface mass balance induced by
763 Antarctic ice rises, *J. Glaciol.*, 60(224), 1101–1110, doi:10.3189/2014JoG14J040, 2014.
- 764 Lenaerts, J. T. M., Lhermitte, S., Drews, R., Ligtenberg, S. R. M., Berger, S. and Helm,
765 V.: Meltwater produced by wind – albedo interaction stored in an East Antarctic ice shelf, *Nat.*
766 *Clim. Chang.*, 7, 58–63, doi:10.1038/NCLIMATE3180, 2017.
- 767 Lindbäck, K., Pettersson, R., Doyle, S. H., Helanow, C., Jansson, P., Kristensen, S. S.,
768 Stenseng, L., Forsberg, R. and Hubbard, A. L.: High-resolution ice thickness and bed topography
769 of a land-terminating section of the Greenland Ice Sheet, *Earth Syst. Sci. Data*, 6, 331–338,
770 doi:doi:10.5194/essd-6-331-2014, 2014.
- 771 Lindbäck, K., Kohler, J., Pettersson, R., Nuth, C. and Langley, K.: Subglacial
772 topography, ice thickness, and bathymetry of Kongsfjorden, northwestern Svalbard, *Earth Syst.*
773 *Sci. Data*, 10, 1769–1781, 2018.
- 774 Makinson, K. and Nicholls, K. W.: Modeling tidal currents beneath Filchner-Ronne Ice
775 Shelf and on the adjacent continental shelf: Their effect on mixing and transport, *J. Geophys.*
776 *Res. Ocean.*, 104(C6), 13449–13465, doi:10.1029/1999jc900008, 1999.
- 777 Malyarenko, A., Robinson, N. J., Williams, M. J. M. and Langhorne, P. J.: A wedge
778 mechanism for summer surface water inflow into the Ross Ice Shelf cavity, *J. Geophys. Res.*
779 *Ocean.*, 1196–1214, doi:10.1029/2018jc014594, 2019.
- 780 Marsh, O. J., Fricker, H. A., Siegfried, M. R., Christianson, K., Nicholla, K. W., Corr, H.
781 F. J. and Catania, G.: High basal melting forming a channel at the grounding line of Ross Ice
782 Shelf, Antarctica, *Geophys. Res. Lett.*, 43, 1–6, doi:10.1002/2015GL066612. Received, 2016.
- 783 Matsuoka, K., Pattyn, F., Callens, D. and Conway, H.: Radar characterization of the basal



- 784 interface across the grounding zone of an ice-rise promontory in East Antarctica, *Ann. Glaciol.*,
785 53(60), 29–34, doi:10.3189/2012AoG60A106, 2012.
- 786 Matsuoka, K., Hindmarsh, R. C. A., Moholdt, G., Bentley, M. J., Pritchard, H. D.,
787 Brown, J., Conway, H., Drews, R., Durand, G., Goldberg, D., Hattermann, T., Kingslake, J.,
788 Lenaerts, J. T. M., Martín, C., Mulvaney, R., Nicholls, K. W., Pattyn, F., Ross, N., Scambos, T.
789 and Whitehouse, P. L.: Antarctic ice rises and rumples: Their properties and significance for ice-
790 sheet dynamics and evolution, *Earth Sci. Rev.*, 150, 724–745,
791 doi:10.1016/j.earscirev.2015.09.004, 2015.
- 792 McGrath, D., Steffen, K., Scambos, T., Rajaram, H., Casassa, G. and Rodriguez Lagos, J.
793 L.: Basal crevasses and associated surface crevassing on the Larsen C ice shelf, Antarctica, and
794 their role in ice-shelf instability, *Ann. Glaciol.*, 53(60), 10–18, doi:10.3189/2012AoG60A005,
795 2012.
- 796 Millgate, T., Holland, P. R., Jenkins, A. and Johnson, H. L.: The effect of basal channels
797 on oceanic ice-shelf melting, *J. Geophys. Res. Ocean.*, 118, 6951–6964,
798 doi:10.1002/2013JC009402, 2013.
- 799 Moholdt, G. and Matsuoka, K.: Inventory of Antarctic ice rises and rumples (version 1), ,
800 doi:10.21334/npolar.2015.9174e644, 2015.
- 801 Mouginot, J., Scheuchl, B. and Rignot, E.: MEaSURES Antarctic Boundaries for IPY
802 2007-2009 from Satellite Radar, Version 2., NASA Natl. Snow Ice Data Cent. Distrib. Act.
803 Arch. Center., doi:<https://doi.org/10.5067/AXE4121732AD>, 2017.
- 804 Mueller, R. D., Padman, L., Dinniman, M. S., Erofeeva, S. Y., Fricker, H. A. and King,
805 M. A.: Impact of tide-topography interactions on basal melting of Larsen C Ice Shelf, Antarctica,
806 *J. Geophys. Res. Ocean.*, 117(5), 1–20, doi:10.1029/2011JC007263, 2012.
- 807 Mueller, R. D., Hattermann, T., Howard, S. L. and Padman, L.: Tidal influences on a
808 future evolution of the Filchner-Ronne Ice Shelf cavity in the Weddell Sea, Antarctica, *Cryosph.*,
809 12(2), 453–476, doi:10.5194/tc-12-453-2018, 2018.
- 810 Natural Resources Canada: CSRS-PPP: On-Line GNSS PPP Post-Processing Service,
811 [online] Available from: <http://webapp.geod.nrcan.gc.ca/geod/tools-ouils/ppp.php>, 2017.



- 812 Nicholls, K. W., Abrahamsen, E. P., Buck, J. J. H., Dodd, P. A., Goldblatt, C., Griffiths,
813 G., Heywood, K. J., Hughes, N. E., Kaletzky, A., Mcphail, S. D., Millard, N. W., Oliver, K. I. C.,
814 Perrett, J., Price, M. R., Pudsey, C. J., Saw, K., Stansfield, K., Stott, M. J., Wadhams, P., Webb,
815 A. T. and Wilkinson, J. P.: Measurements beneath an Antarctic ice shelf using an autonomous
816 underwater vehicle, *Geophys. Res. Lett.*, 33, doi:10.1029/2006GL025998, 2006.
- 817 Nicholls, K. W., Corr, H. F. J., Stewart, C. L., Lok, L. B., Brennan, P. V and Vaughan, D.
818 G.: Instruments and Methods A ground-based radar for measuring vertical strain rates and time-
819 varying basal melt rates in ice sheets and shelves, *J. Glaciol.*, 61(230), 1079–1087,
820 doi:10.3189/2015JoG15J073, 2015.
- 821 Nøst, O. A., Biuw, M., Tverberg, V., Lydersen, C., Hattermann, T., Zhou, Q., Smedsrud,
822 L. H. and Kovacs, K. M.: Eddy overturning of the Antarctic Slope Front controls glacial melting
823 in the Eastern Weddell Sea, *J. Geophys. Res. Ocean.*, 116(11), 1–17,
824 doi:10.1029/2011JC006965, 2011.
- 825 Padman, L., Siegfried, M. R. and Fricker, H. A.: Ocean Tide Influences on the Antarctic
826 and Greenland Ice Sheets, *Rev. Geophys.*, 56(1), 142–184, doi:10.1002/2016RG000546, 2018.
- 827 Paolo, F. S., Fricker, H. A. and Padman, L.: Volume loss from Antarctic ice shelves is
828 accelerating, *Science*, 348(6232), 327–332, 2015.
- 829 Pritchard, H. D., Ligtenberg, S. R. M., Fricker, H. A., Vaughan, D. G., Broeke, M. R.
830 Van Den and Padman, L.: Antarctic ice-sheet loss driven by basal melting of ice shelves, *Nature*,
831 484(7395), 502–505, doi:10.1038/nature10968, 2012.
- 832 Rahman, S.: FMCW Radar Signal Processing for Antarctic Ice Shelf Profiling and
833 Imaging, University College London., 2016.
- 834 Reese, R., Gudmundsson, G. H., Levermann, A. and Winkelmann, R.: The far reach of
835 ice-shelf thinning in Antarctica, *Nat. Clim. Chang.*, 8, 53–57, doi:10.1038/s41558-017-0020-x,
836 2018.
- 837 Rignot, E., Mouginot, J. and Scheucht, B.: Ice Flow of the Antarctic Ice Sheet, *Science*,
838 333, 1427–1431, 2011.
- 839 Rignot, E., Jacobs, S., Mouginot, J. and Scheuchl, B.: Ice-Shelf Melting Around



- 840 Antarctica, *Science*, 341, 266–270, 2013.
- 841 Rignot, E., Mouginot, J., Morlighem, M., Seroussi, H. and Scheuchl, B.: Widespread,
842 rapid grounding line retreat of Pine Island, Thwaites, Smith, and Kohler glaciers, West
843 Antarctica, from 1992 to 2011, *Geophys. Res. Lett.*, 3502–3509,
844 doi:10.1002/2014GL060140. Received, 2014.
- 845 Rignot, E., Mouginot, J., Scheuchl, B., van den Broeke, M. R., van Wessem, M. J. and
846 Morlighem, M.: Four decades of Antarctic Ice Sheet mass balance from 1979–2017, *Proc. Natl.*
847 *Acad. Sci.*, 1–9, doi:10.1073/pnas.1812883116, 2019.
- 848 Rintoul, S. R., Silvano, A., Pena-molino, B., Wijk, E. Van, Rosenberg, M., Greenbaum,
849 J. S. and Blankenship, D. D.: Ocean heat drives rapid basal melt of the Totten Ice Shelf, *Sci.*
850 *Adv.*, 2, 1–5, 2016.
- 851 Ryan, S., Schröder, M., Huhn, O. and Timmermann, R.: On the warm inflow at the
852 eastern boundary of the Weddell Gyre, *Deep. Res. Part I Oceanogr. Res. Pap.*, 107, 70–81,
853 doi:10.1016/j.dsr.2015.11.002, 2016.
- 854 De Santis, A., Maier, E., Gomez, R. and Gonzalez, I.: Antarctica, 1979–2016 sea ice
855 extent: total versus regional trends, anomalies, and correlation with climatological variables, *Int.*
856 *J. Remote Sens.*, 38(24), 7566–7584, doi:10.1080/01431161.2017.1363440, 2017.
- 857 Schmidtko, S., Heywood, K. J., Thompson, A. F. and Aoki, S.: Multidecadal warming of
858 Antarctic waters: Supplementary Material, *Science*, 346(6214), 1227–1231,
859 doi:10.1126/science.1256117, 2014.
- 860 Schreiber, T. and Schmitz, A.: Surrogate time series, *Phys. D*, 142, 346–382, 2000.
- 861 Shepherd, A., Fricker, H. A. and Farrell, S. L.: Trends and connections across the
862 Antarctic cryosphere, *Nature*, 558, 223–232, 2018.
- 863 Stanton, T. P., Shaw, W. J., Truffer, M., Corr, H. F. J., Peters, L. E., Riverman, K. L.,
864 Bindshadler, R. A., Holland, D. M. and Anandakrishnan, S.: Channelized Ice Melting in the,
865 *Science*, 341(September), 1236–9, doi:10.1126/science.1239373, 2013.
- 866 Stern, A. A., Dinniman, M. S., Zagorodnov, V., Tyler, S. W. and Holland, D. M.:
867 Intrusion of warm surface water beneath the McMurdo ice shelf, Antarctica, *J. Geophys. Res.*



- 868 Ocean., 118(12), 7036–7048, doi:10.1002/2013JC008842, 2013.
- 869 Stewart, A. L. and Thompson, A. F.: Eddy Generation and Jet Formation via Dense
870 Water Outflows across the Antarctic Continental Slope, *J. Phys. Oceanogr.*, 46(12), 3729–3750,
871 doi:10.1175/jpo-d-16-0145.1, 2016.
- 872 Stewart, C. L., Christoffersen, P., Nicholls, K. W., Williams, M. J. M. and Dowdeswell,
873 J. A.: Basal melting of Ross Ice Shelf from solar heat absorption in an ice-front polynya, *Nat.*
874 *Geosci.*, 1(January), doi:10.1038/s41561-019-0356-0, 2019.
- 875 Stuecker, M., Bitz, C. and Armour, K.: Conditions leading to the unprecedented low
876 Antarctic sea ice extent during the 2016 austral spring season, *Geophys. Res. Lett.*, 44, 9008–
877 9019, doi:10.1002/2017GL074691. Received, 2017.
- 878 Sverdrup, H. U.: The Currents off the Coast of Queen Maud Land, *Nor. Geogr. Tidsskr. -*
879 *Nor. J. Geogr.*, 14(1–4), 239–249, doi:10.1080/00291955308542731, 1954.
- 880 Swart, N. C., Gille, S. T., Fyfe, J. C. and Gillett, N. P.: Recent Southern Ocean warming
881 and freshening driven by greenhouse gas emissions and ozone depletion, *Nat. Geosci.*, 11, 836–
882 842, doi:10.1038/s41561-018-0226-1, 2018.
- 883 Taylor, J. R.: *An Introduction to Error Analysis: The Study of Uncertainties in Physical*
884 *Measurements*, University of Colorado., 1996.
- 885 The IMBIE Team: Mass balance of the Antarctic Ice Sheet from 1992 to 2017, *Nature*,
886 558, 219–222, doi:10.1017/cbo9780511535659.014, 2018.
- 887 Thompson, A. F., Heywood, K. J., Schmidtko, S. and Stewart, A. L.: Eddy transport as a
888 key component of the Antarctic overturning circulation, *Nat. Geosci.*, 7(12), 879–884,
889 doi:10.1038/ngeo2289, 2014.
- 890 Thompson, A. F., Stewart, A. L., Spence, P. and Heywood, K. J.: The Antarctic Slope
891 Current in a Changing Climate, *Rev. Geophys.*, 56(4), 741–770, doi:10.1029/2018RG000624,
892 2018.
- 893 Turner, J., Hosking, J. S., Bracegirdle, T. J., Marshall, G. J. and Phillips, T.: Recent
894 changes in Antarctic Subject Areas, *Philos. Trans. R. Soc. London, A* 373(20140163), 2015.
- 895 Turner, J., Lu, H., White, I., King, J. C., Phillips, T., Hosking, J. S., Bracegirdle, T. J.,



- 896 Marshall, G. J., Mulvaney, R. and Deb, P.: Absence of 21st century warming on Antarctic
897 Peninsula consistent with natural variability, *Nature*, 535, 411, 2016.
- 898 Vaňková, I., Voytenko, D., Nicholls, K. W., Xie, S., Parizek, B. R. and Holland, D. M.:
899 Vertical Structure of Diurnal Englacial Hydrology Cycle at Helheim Glacier, East Greenland,
900 *Geophys. Res. Lett.*, 45(16), 8352–8362, doi:10.1029/2018GL077869, 2018.
- 901 Zhou, Q., Hattermann, T., Nøst, O. A., Biuw, M., Kovacs, K. M. and Lydersen, C.:
902 Wind-driven spreading of fresh surface water beneath ice shelves in the Eastern Weddell Sea, *J.*
903 *Geophys. Res. Ocean.*, 3818–3833, 2014.